Nuclear Inst. and Methods in Physics Research, A 925 (2019) 24–32

Contents lists available at ScienceDirect

Nuclear Inst. and Methods in Physics Research, A

journal homepage: www.elsevier.com/locate/nima

A new beamline for laser spin-polarization at ISOLDE

W. Gins [a,*], R.D. Harding [b,c], M. Baranowski [d], M.L. Bissell [e], R.F. Garcia Ruiz [a,1], M. Kowalska [b], G. Neyens [a,b], S. Pallada [b], N. Severijns [a], Ph. Velten [a], F. Wienholtz [b], Z.Y. Xu [a], X.F. Yang [a,f], D. Zakoucky [g]

[a] KU Leuven, Instituut voor Kern- en Stralingsfysica, Leuven, Belgium
[b] EP Department, CERN, Switzerland
[c] University of York, York, United Kingdom
[d] Faculty of Physics, Adam Mickiewicz University, Poznan, Poland
[e] School of Physics and Astronomy, The University of Manchester, Manchester, United Kingdom
[f] School of Physics and State Key Laboratory of Nuclear Physics and Technology, Peking University, Beijing 100871, China
[g] NPI, Czech Academy of Sciences, Rez, Czech Republic

ARTICLE INFO

Keywords:
Beamline
Laser polarization
β-asymmetry
Adiabatic rotation

ABSTRACT

A beamline dedicated to the production of laser-polarized radioactive beams has been constructed at ISOLDE, CERN. We present here different simulations leading to the design and construction of it, as well as technical details of the full setup and examples of the achieved polarizations for several radioisotopes. Beamline simulations show a good transmission through the entire line, in agreement with observations. Simulations of the induced nuclear spin-polarization as a function of atom–laser interaction length are presented for ^{26,28}Na, and for ^{35}Ar, which is studied in this work. Adiabatic spin rotation calculations of the spin-polarized ensemble of atoms, and how this influences the observed nuclear ensemble polarization, are also performed for the same nuclei. For ^{35}Ar, we show that multiple-frequency pumping enhances the ensemble polarization by a factor 1.85, in agreement with predictions from a rate equations model.

1. Introduction

Spin-polarized radioactive nuclei have been a staple of nuclear and particle physics research since the discovery of parity violation [1]. With the use of polarized nuclei as a probe in fields ranging from fundamental interactions to material and life sciences [2–5], an initiative for a dedicated experiment at ISOLDE was started, and a beamline was built and commissioned. Results from the commissioning of the new beamline have been reported in Ref. [6]. The present article documents the technical aspects of this beamline.

Section 2 describes the mechanism of laser polarization through optical pumping and how the induced nuclear polarization can be observed through the asymmetry in the nuclear β-decay. Section 3 reports on the different parts of the beamline, with Section 4 being dedicated to the ion-optical simulations. The magnetic field configuration along the beamline is discussed in Section 5. Calculations of the adiabatic rotation of the spin-polarized ensembles of ^{26,28}Na and ^{35}Ar in the magnetic fields are presented in Section 6 and compared to the observed asymmetries. The successful use of multiple-frequency optical pumping to achieve higher polarization for ^{35}Ar atoms, to be used in future fundamental interactions studies [4], is described in Section 7 and compared with experimental data. Conclusions are given in Section 8.

2. Optical pumping and β-asymmetry

The hyperfine interaction couples the nuclear spin $\vec{I}$ and the electron spin $\vec{J}$ together to a total atomic spin $\vec{F} = \vec{I} + \vec{J}$, which splits a fine structure level, characterized by the J quantum numbers into several hyperfine levels characterized by the F quantum numbers. Atomic population can be resonantly transferred from one hyperfine level to a radiatively coupled level through interaction with a narrowband laser. Typically, a continuous wave (cw) laser is used. In this process, conservation of angular momentum dictates that the atomic spin $\vec{F}$ can only change by maximally one unit. The left side of Fig. 1 illustrates the five allowed hyperfine transitions for the D2 line in ^{28}Na ($3^2S_{1/2} \rightarrow 3^2P_{3/2}$) as solid lines. The term "optical pumping" is used when resonant excitations and decay drive the atomic population towards a specific (magnetic sub)state [7].

When the laser light is circularly polarized (σ^+ or σ^-), conservation of angular momentum further imposes the restriction $\Delta m_F = 1$ or -1 (indicated as solid lines on the right side of Fig. 1). The decay back to the lower state is however not bound to this rule and can proceed with $\Delta m_F = 0, \pm 1$ (indicated by dashed lines) [8]. By repeating such

* Corresponding author.
E-mail addresses: wouter.gins@fys.kuleuven.be (W. Gins), robert.harding@cern.ch (R.D. Harding).
[1] Current affiliation: EP Department, CERN, CH-1211 Geneva 23, Switzerland.

https://doi.org/10.1016/j.nima.2019.01.082
Received 24 September 2018; Received in revised form 25 January 2019; Accepted 25 January 2019
Available online 5 February 2019

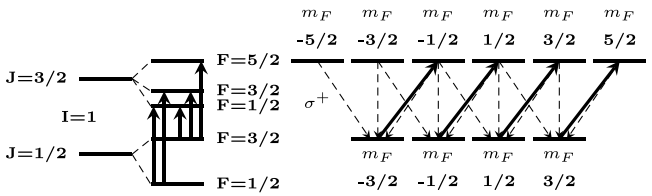

Fig. 1. Optical pumping scheme in the D2 line of ^{28}Na. Excitations using σ^+ polarized light are drawn with solid lines, while the dashed lines indicate decay paths through photon emission.

excitation/decay cycles many times, the population of a specific F-state is pushed towards substates with either maximal or minimal m_F quantum numbers in the initial state.

The number of excitation/decay cycles can be increased by either increasing the laser photon density or by having a longer interaction time. In a collinear geometry (as used in high-resolution collinear laser spectroscopy experiments [9]), where the particle and cw laser beam are spatially overlapped, such a long interaction time is achieved by choosing an appropriate length of the laser–particle interaction region.

The resulting atomic polarization is then transferred to a polarization of the nuclear spins through the hyperfine interaction. The nuclear polarization in such an ensemble of nuclei is defined as

$$P = \sum_{m_I} \frac{w\left(m_I\right) m_I}{I}, \tag{1}$$

with $w\left(m_I\right)$ the probability that the $\left|I, m_I\right\rangle$ quantum state is populated after the optical pumping process.

The nuclear polarization can be observed by detecting the asymmetry in the β-decay of radioactive isotopes, due to the parity violation in nuclear β-decay [1]. The β-decay of a polarized ensemble has a specific angular distribution that can be approximated to $W(\theta) \sim 1 + AP\cos(\theta)$ for allowed β-transitions [10], where θ is the angle between the emitted electron momentum and the nuclear spin orientation. A is the asymmetry parameter of the decay which depends on the initial and final spin of the nuclear states involved in the β-decay, and P is the polarization of the nuclear ensemble with respect to a quantization axis. The experimental asymmetry (as reported in Section 7) is then defined as

$$A_{exp} = \frac{N(0°) - N(180°)}{N(0°) + N(180°)} = \epsilon AP, \tag{2}$$

where ϵ represents depolarization effects which depend on several experimental factors.

For more details on spin-polarization via optical pumping, see Refs. [11,12].

3. Beamline description

More than 1300 radioactive isotopes of more than 70 elements can be produced at ISOLDE, CERN, via the impact of a 1.4 GeV proton beam on a variety of targets using different types of ion sources [13]. The resulting ion beam is mass-separated in the High Resolution Separator (HRS) after which it can be bunched, if desired, using the ISCOOL cooler-buncher [14]. After mass separation, the ion beam is sent to the laser-polarization setup, which is part of the Versatile Ion Techniques Online (VITO) beamline at ISOLDE, CERN [15]. For ions or atoms having a suitable scheme for laser optical pumping, typically the alkaline and alkaline-earth elements, the nuclear spin of the isotopes can be polarized through application of optical pumping of an atomic hyperfine transition. The ion beam from ISOLDE is sent into the laser-polarization beamline and overlapped with a circularly polarized laser beam to induce nuclear polarization. After implantation in a suitable host, placed in a strong magnetic field, the change in β-asymmetry is observed as a function of laser frequency, scanned across the hyperfine structure. Although the technique is also applicable to ions [16], the current design is specific for working with atoms. An overview of the layout of the entire optical pumping beamline is shown in Fig. 2.

The first element of the beamline is a 5° deflector equipped with a laser window, where the laser beam is overlapped with the pulsed radioactive ion beam. A beam diagnostics box, containing an adjustable iris to define the beam waist and a readout plate for the ion-current, is placed directly after the deflector. Beamline simulations of the 5° deflector are discussed in Section 4.

The Charge Exchange Cell (CEC), housed in the Charge Exchange vacuum chamber of Fig. 2 and depicted in Fig. 3, is placed after the diagnostic box, where the beam passes through a vapor of Na or K and undergoes charge exchange. It contains a reservoir in the middle where solid Na or K is deposited. The stainless steel reservoir is heated using six RS Components RS-8607016 220 W heating cartridges powered by a DC power supply. The reservoir is heated to approximately 200 °C for both Na and K in order to produce a sufficiently dense vapor for charge exchange [17,18]. Neutralization efficiencies of 100% for a Na^+ beam on Na vapor and 50%–75% for an Ar^+ beam on K vapor have been observed. To minimize diffusion of the Na or K vapor into the rest of the beamline, the ends of the pipe are kept at a lower temperature. This is achieved using a heatsink cooled with circulating Galden® PFPE of 90° C, which keeps the ends of the beampipe at about 100° C, above the melting point of K (63.2 °C) and Na (97.8 °C). The lower temperature condenses the vapor into a liquid which flows back to the center. This minimizes the loss of vapor to the rest of the beamline and ensures a high vapor density in the middle. Non-neutralized ions are deflected from the beam after the CEC using an electrostatic deflector. A specially designed electrode arrangement (referred to as *voltage scanner*, design details in

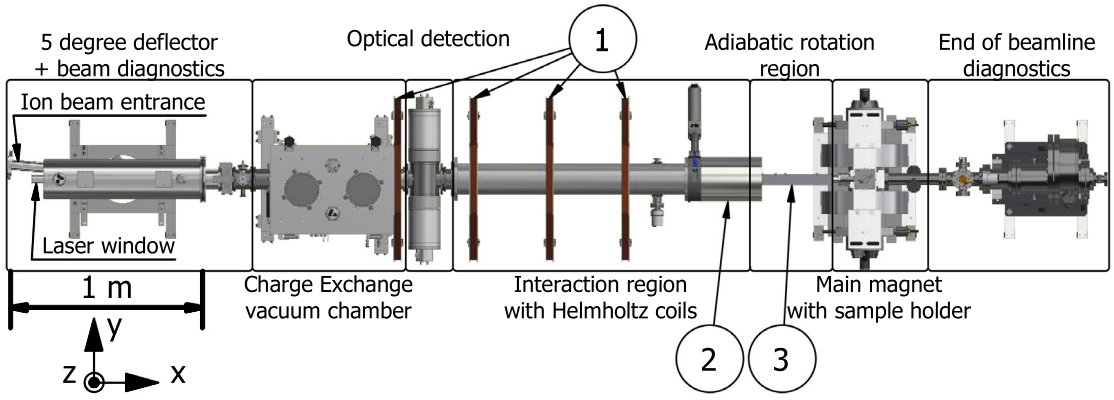

Fig. 2. Schematic overview of the VITO beamline, with the main beamline components indicated. The beam from ISOLDE enters from the top left beampipe, and the start of this beampipe is used as the start for the ion-optical simulations. The numbers are used to indicate the coils in Table 1. Indicated in the bottom left is the axis system used throughout this paper.

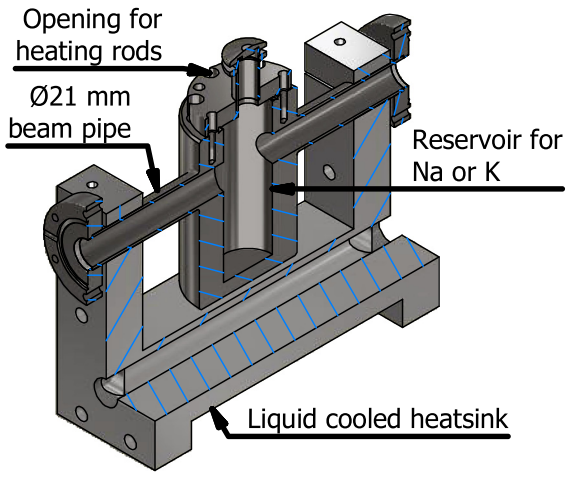

Fig. 3. 3/4 view of the CAD drawing of the CEC. The stainless steel reservoir has 6 deep holes to house heating rods. The liquid cooled heatsink clamps onto the beampipe ends.

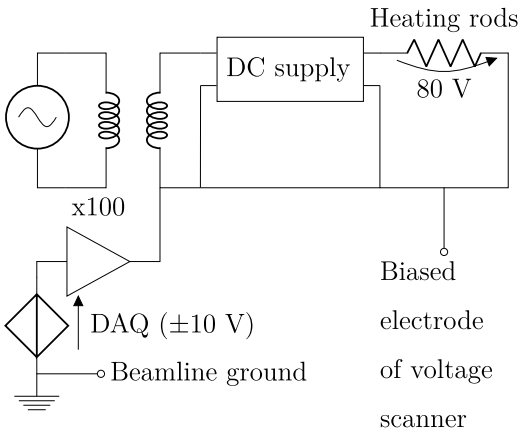

Fig. 4. Simplified diagram of the electrical wiring for the voltage scanning. The voltage scanning provides a floating potential for a secondary circuit, where an isolating transformer supplies power to a DC power supply for the heating rods mentioned in Section 3. The data acquisition program can supply ±10V, which is amplified by a factor 100.

Section 4) is attached to this cell and modifies the kinetic energy of the incoming ion beam. This changes the velocity of the beam, and induces a Doppler shift of the laser frequency. The relation between the labframe ν_{rest} frequency and the frequency ν_{obs} observed by this accelerated (or decelerated) beam is

$$\nu_{obs} = \nu_{rest}\sqrt{\frac{1-\beta}{1+\beta}}, \tag{3}$$

$$\beta = \sqrt{1-\left[mc^2/\left(mc^2+qE_{kin}\right)\right]^2}, \tag{4}$$

where m and q are the mass and charge of the particles, c is the speed of light and E_{kin} is the kinetic energy. This allows a fast scanning of the hyperfine structure by changing the acceleration voltage. In Fig. 4 we show the electrical diagram of the wiring that enables this voltage scanning. The data acquisition system (DAQ) contains a digital-to-analog converter (DAC) and can provide a controlled voltage of up to ±10 V, which is amplified by a Kepco amplifier (model number BOP 1000M, modified for high inductive loads) by a factor of 100. This voltage of ±1 kV (and typical precision of 0.02 V) is then applied to the secondary windings of an isolating transformer. The insulating transformer supplies the 230 V line voltages on the secondary side to a DC power supply which is then also floated by the ±1 kV. Since the biased electrode of the voltage scanner is connected to the base of the CEC and thus to the lower output of the power supply, both elements are biased to ±1 kV relative to the beamline ground while a constant voltage is applied over the heating rods.

Following the CEC is the optical detection region, which is a copy of the light collection region used in the COLLAPS setup [19]. The photomultiplier tubes in this detection area are used for determining the resonant laser frequency through optical detection of the fluorescence decay from a stable isotope of the same element, prior to starting β-asymmetry measurements on the less abundant radioactive species of interest.

In the interaction region, where the optical pumping takes place, Helmholtz coils provide a magnetic field on the order of 2 mT along the beamline axis pointing in the beam direction. This magnetic field defines a quantization axis and avoids coupling of the atomic spins to possible stray fields in the environment. The minimal length of this interaction region is determined by the time needed for the pumping process. The process of optical pumping with a cw laser can be modeled through the formation of rate equations based on the Einstein formalism [11,20,21]. By solving this system of differential equations, the degree of nuclear polarization P (Eq. (1)) can be calculated for any interaction time.

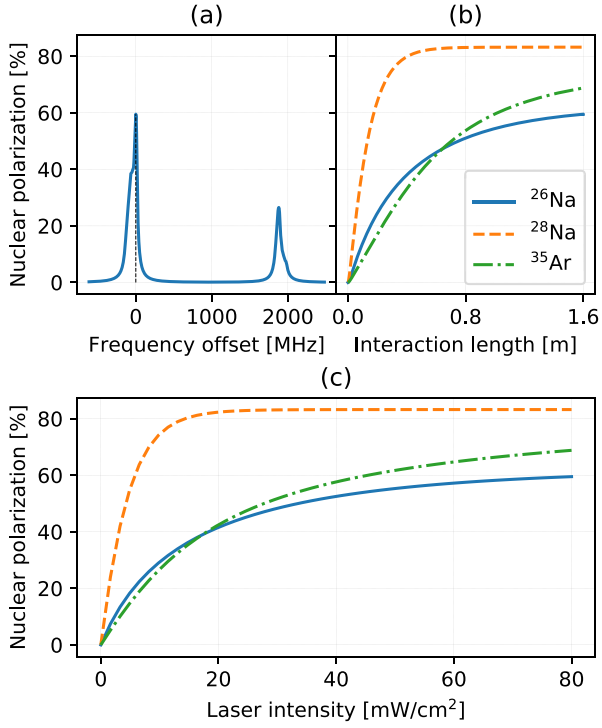

Fig. 5. (a) Simulated hyperfine spectrum for pumping ^{26}Na in the D2 line using σ+ polarized light at a typical laser power of 80 mW/cm^2. The interaction time corresponds to an interaction length of 1.6 m for a 50 keV beam. (b) The calculated polarization in the strongest component of the hyperfine spectrum (indicated with a dashed line in (a)) as a function of interaction length for the different nuclear species discussed in this paper. (c) The laser intensity dependence of the strongest component of the hyperfine spectrum for an interaction length of 1.6 m.

The D2 line in Na [6] was used as the case study. Fig. 5(a) shows the hyperfine spectrum generated with this method, while in (b) the polarization in the most intense peak is calculated as a function of the laser–atom interaction time (translated into a beamline length assuming a 50 keV beam). In both figures, a laser intensity of 80 mW/cm^2 was used as this is a typically achievable power density. Calculation of the polarization as a function of laser intensity is shown in Fig. 5(c), demonstrating that the transition is saturated in the simulation. The difference in maximal polarization for the different nuclei is due to the number of hyperfine levels across which the population is distributed

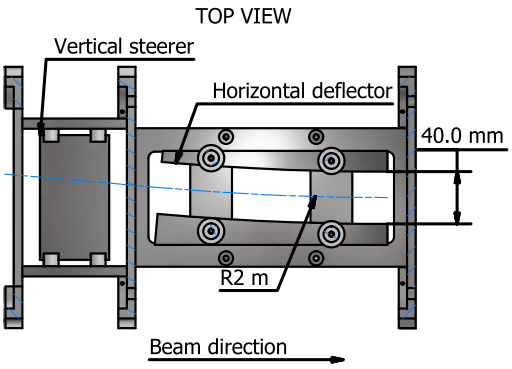

Fig. 6. CAD drawing of the 5° ion-deflector. Ion beam coming from ISOLDE (left) is bent 5°s with a radius of 2 m to overlap the ion beam with the laser beam.

originally. Based on these calculations, a length of 1.6 m was selected as a compromise between achievable polarization and available space in the ISOLDE hall. Although the length needed to fully polarize an ensemble depends on the Einstein A parameter of the transition, 1.6 m will give a sufficiently long interaction time for most strong transitions for which A has a value in the order of $10^7 - 10^8$ Hz. This is illustrated in Fig. 5(b) for ^{26,28}Na and ^{35}Ar, the first isotopes that have been polarized with the new set-up.

A series of solenoids and a large electromagnet are placed after the interaction region, with the field of the solenoids acting along the beam direction and the electromagnet generating a field perpendicular to it. The combination of these fields adiabatically rotates the atomic spin in the horizontal plane, orienting it in the same direction as the field of the electromagnet. This field is sufficiently strong to decouple the nuclear from the electron spin. The details of this adiabatic spin rotation and decoupling of the nuclear and electron spins are discussed in Section 6. A removable sample holder and β-detectors are installed inside the electromagnet, where the polarized ensemble is implanted in a suitable host material. This β-detection setup has been used before in β-NMR studies on Mg isotopes [16].

A diagnostics box containing a wire scanner and Faraday cup, as detailed in [13] (supplemented with a copper plate to detect atomic beams), is installed after this region to provide beam diagnostics.

4. Ion optics

Ion-optical beam transmission simulations were performed to benchmark the effect that the deflector and voltage scanner have on the path of the beam and the transmission that can be expected.

A standard beam of $^{39}K^{+}$ with 3 π mm mrad beam emittance is generated for the simulations, as reported for the cooler-buncher ISCOOL [14]. The focal point of the beam is, prior to entering the 5° deflector, optimized for maximal transmission using the quadrupole doublet that is installed in front of it. As the doublet is not included in the simulations, the focus is set by optimizing the Twiss parameters in the simulation. For Gaussian beams, the distribution in phase space is given by an ellipse, where the orientation and shape is given by the Twiss parameters [22]. Changing these parameters changes both the size of the beam, as well as the focal point. The kinetic energy of the beam is set to 60 keV, which is the maximal beam energy that can be delivered by ISOLDE to the low energy section. For all simulations, the COMSOL multiphysics software was used [23]. The used geometry is a simplified version of the geometry shown in Fig. 2. First an overview of all the elements included in the simulations will be given.

The first electrostatic element of the VITO beamline in the simulations is the 5° deflector, which bends the ion beam to overlap it collinearly with the laser light. The 5° deflector has an internal opening of 40 mm and consists of two vertical steerer plates and a pair of electrodes with a machined curve matching 2 m (see Fig. 6). After this, a voltage scanner (the design of which will be treated further in this section) adjusts the kinetic energy of the ion beam in a range of ±1 keV. It is mounted inside the vacuum box where the CEC is also mounted and the biased electrode is connected to the CEC. The CEC acts as a long collimator with a 2 cm opening, followed by another collimator with an opening of 1 cm approximately 2 m further downstream. These small collimators guarantee a good overlap between the particle and laser beam. As the charge exchange process neutralizes the charged particles, the CEC is the final electrostatic element considered in the simulations. The tubes and chambers forming the beamline up to this point are also present and are grounded to provide accurate potential fields.

The design for the voltage scanner deviates from a series of ring electrodes connected through a resistor chain [21]. Instead, two specially shaped electrodes define the equipotential electrical field (Fig. 7(a)). Two configurations of this geometrical design of the shaped electrodes have been used.

In the first configuration (Config. 1 in Fig. 7(a)), eight triangular spikes are attached to an octagonal mounting base. Overlapping two of such electrodes gives a gradual and nearly-linear change in potential experienced by the ions, as shown in Fig. 7(b). In the second design (Config. 2 in Fig. 7(a)), the grounded electrode is replaced with a cylinder covering the entire scanner, separated from the biased electrode with a teflon insulator. The central beam axis thus is more fully encapsulated and has a better defined ground potential, resulting in a more sigmoidal variation of the electric potential (Fig. 7(c)). To emulate mechanical imperfections related to the construction, the grounding electrode was rotated 0.5° relative to the z-axis as defined in Fig. 2. This rotation is implemented in all simulations for both configurations (Fig. 7(a)). The typical flight path of the particles is depicted in Fig. 8, where the extent of the particle beam is given. The collimators are visible as the sharp cuts at 3 and 7 μs.

The transmission of the beam through the beamline as a function of scanning voltage has been simulated for the two different designs of the voltage scanner (Fig. 9a). A second set of simulations were performed with a slightly detuned 5° deflector (Fig. 9b). Both designs have been constructed and used in experiments, such that the transmission simulations can be compared to actual data (Fig. 9c).

The transmission data for the first configuration was gathered in the commissioning experiment [6] by means of the total β-counts from a ^{26}Na beam measured as a function of scanning voltage. During an experiment on β-NMR in liquid samples performed in May 2018 [3], the second configuration was used for the first time and the data was gathered in the same way.

The simulations (top two panels of Fig. 9) and the online data (bottom panel of Fig. 9) show very good agreement. The oscillation in the counts is due to the proton supercycle. Proton pulses are separated by an integer number of 1.2 s, but the time between subsequent pulses can vary. A rapid succession of pulses causes build-up and a variation in yield, which can only be averaged away by measuring over many supercycles. In both the measurements and the simulations, the first configuration has a severe beamsteering effect, reducing the transmission efficiency as a function of scanning voltage. The second configuration has no such effect, owing to the better ground potential definition. The simulations with a detuned 5° deflector show that this can result in a slight slope for the second configuration and a shift in the peak location for the first. These features are also present in the data.

Based on comparisons of the beam current on Faraday cups located before and at the end of the beamline, a maximal transmission of ~60% was observed in May 2018. As this transmission is heavily dependent on the exact emittance of the beam, this small deviation from the simulated value of 75% is not unreasonable.

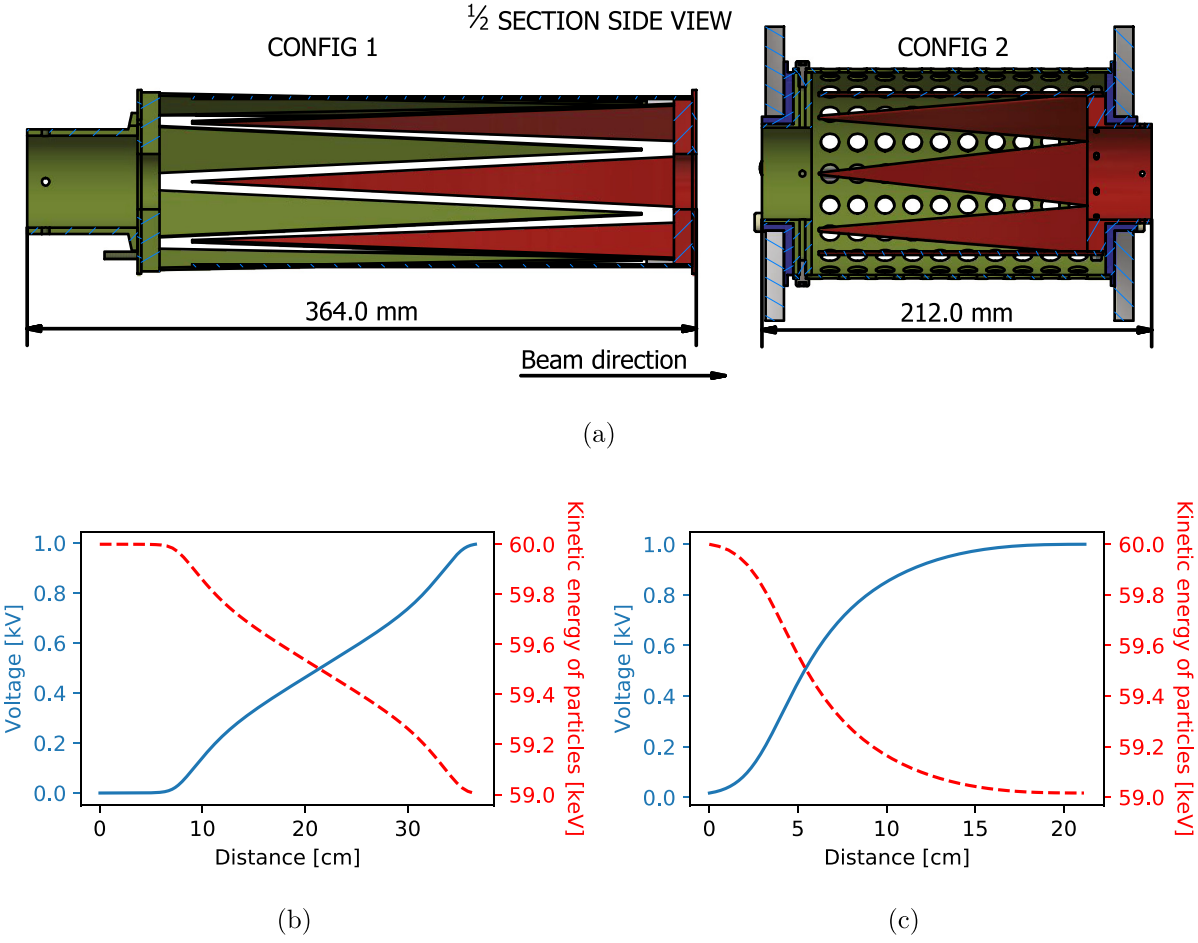

Fig. 7. (a) 1/2 section view of both configurations for the voltage scanner. The biased electrode is indicated in red, the grounded electrode in green and the teflon insulator in blue. (b) Electric potential (full line) and the kinetic energy (dashed line) of a 60 keV beam of ^{39}K as a function of distance using configuration 1 when 1 kV is applied to the biased electrode. (c) Same as (b), but for configuration 2 . (For interpretation of the references to color in this figure legend, the reader is referred to the web version of this article.)

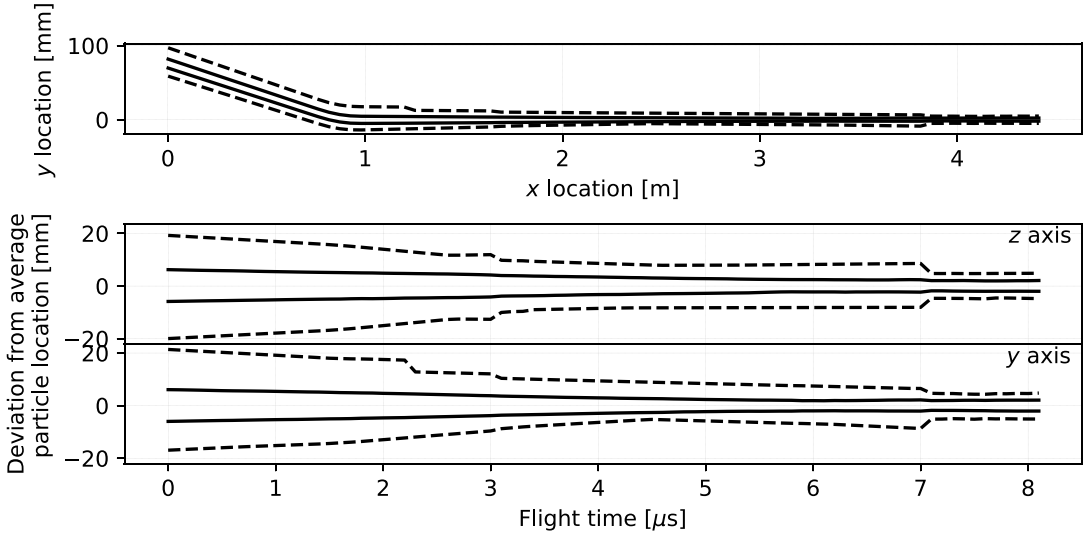

Fig. 8. Overview of the particle trajectories as a function of x and y location (top panel), and as a function of flight time and deviation from the center of the beam in the y and z directions (bottom two panels). The solid black lines indicate the area containing $\pm 1\sigma$ of the beam, the dashed lines the location of the outermost particles The focal point corresponds to the location at $x \approx 3.5$ m, at a flight time of 6 μs. The axis system is the same one as used in Fig. 2.

5. Design of magnetic fields

The magnetic field generated in the beamline is separated in three separate sections (see Fig. 2), each with their own requirements:

1. the interaction region (labeled 1 and 2 in Fig. 2).
2. the transitional field region (labeled 3).
3. the main magnet region.

Table 1
Optimized parameters for the coils as determined with COMSOL simulations. A wire thickness of 0.8 mm was used through all simulations. For the Helmholtz coils, the radius refers to the inscribed circle. The length refers to the dimension of the coil along the beamline axis. The number after the description refers to the labeling in Fig. 2.

	Helmholtz coils (1)	Large solenoid (2)	Small solenoids (3)				
			1	2	3	4	5
Current [A]	1.6	1.0	2				
Windings [#]	1000	900	10	65	154	1100	225
Radius [mm]	400	112.5	20.5				
Length [mm]	32	315	40	60	40	154	66

The interaction region has to provide a weak, uniform magnetic field over the entire beam path that needs to compensate for stray fields in order to maintain the laser-induced atomic spin polarization. The field should be small enough however, not to induce a large splitting of the magnetic substates of the hyperfine levels. A magnetic field of approximately 2 mT fulfills both requirements.

Once the radioactive beam is implanted, the magnetic field has to be strong enough to decouple the nuclear spin from random interactions with potential (defect-associated) electric field gradients in the crystal. The installed electromagnet can generate a field of up to 0.7 T. This value depends on both the current supplied to the magnet as well as the distance between the magnet poles, which can be varied. With a maximal pole distance of 8 cm, different setups for holding samples and placing detectors can be accommodated.

Since the field generated by the electromagnet is perpendicular to the beamline axis (which is also the atomic spin orientation axis), the transitional field region has to be tuned to provide adiabatic rotation of the oriented atomic spins. The field previously designed for the β-NMR setup at COLLAPS (see Ref. [24]) was used as a model for this.

For designing the magnetic field of both the interaction and the transitional region, simulations were made in COMSOL. As a design choice, four octagonal coils arranged in a Helmholtz configuration are used for the interaction region (see Fig. 2). The light guides of the β-detection system prevents us from putting a fifth octagonal coil. Therefore, a solenoid with 11.25 cm radius extends the interaction region. Several smaller solenoids directly wound onto a beampipe continue past this point and form the transitional field. The final parameters of all solenoids are given in Table 1.

In order to compare the simulated magnetic field profile with reality, magnetic field measurements with a 3D Hall probe were made in three circumstances: the transitional field and the electromagnet on (red wide diamonds in Fig. 10), only the main magnet powered (green dots) and only the transitional field powered (blue thin diamonds). Due to the unknown configuration in the main magnet, only the transitional field could be simulated in COMSOL (full line). The good agreement between simulation and measurements suggests a good correspondence between the coil parameters in the simulation and the physical coils.

6. Adiabatic rotation

In the experimental set-up, the atomic spin-polarization axis is along the (laser) beamline. On the other hand, for the β-asymmetry measurements, the nuclear spin-polarization axis should be along the direction of the strong holding field in which the implantation crystal is mounted. This field is perpendicular to the beamline, in order to allow for β-detectors to be mounted at 0 and 180 degrees with respect to the field direction. From the rate equation calculations of the atomic population, the nuclear spin polarization is extracted under the assumption that the decoupling field is oriented along the spin-polarization axis. As we apply a gradually increasing magnetic field in order to rotate (and decouple) the nuclear and electron spins adiabatically into the strong field direction, changes in the nuclear spin polarization due to the adiabatic rotation process are possible. To this end, simulations of this

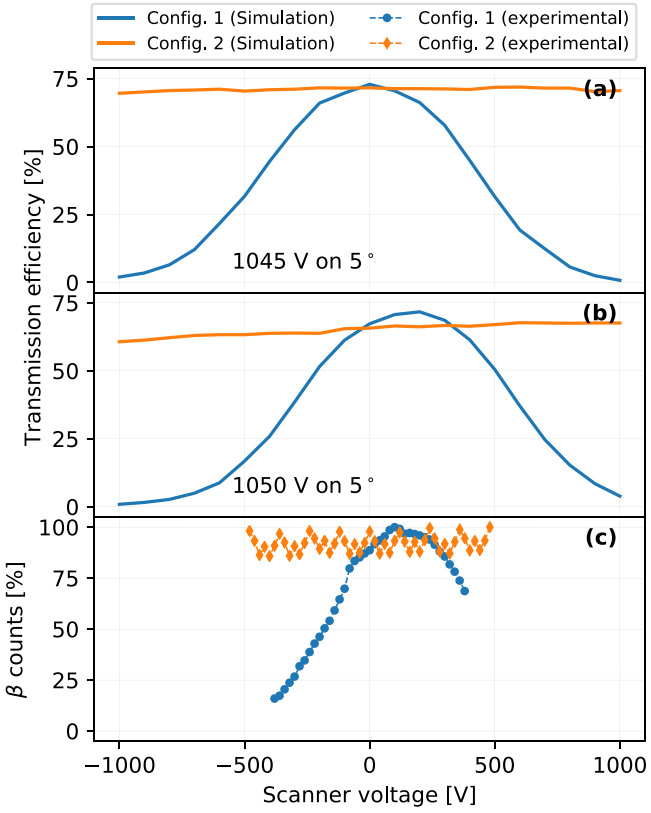

Fig. 9. Transmission efficiency through the beamline, simulated for both configurations of the scanning electrodes, as a function of voltage applied to the scanner and for two different voltages on the deflector. When the optimal voltage is applied to the 5° deflector (1045 V, (a)), the beam is centered on the axis of the biased electrode, while a slightly offset voltage (1050 V, (b)) results in slightly lower transmission since the axes of the beam and the electrode no longer coincide. The experimental transmission profile (c) agrees with the general trend predicted by the simulations. The β-counts have been normalized to the datapoint with the highest intensity, the staggering in the data is due to the structure of the proton beam supercycle.

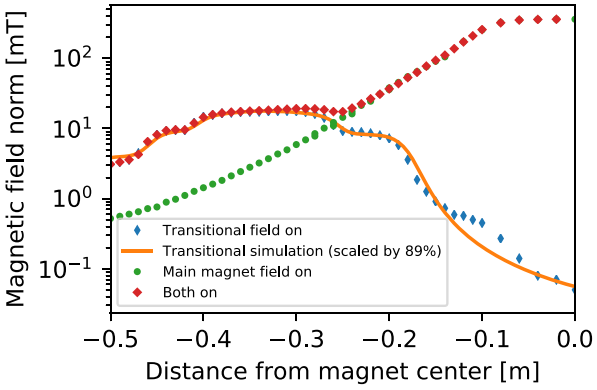

Fig. 10. Comparison between the simulation (solid line) and measurements (markers) of the magnetic field. The simulation is scaled down by a global factor to account for a difference between the read-out current and the current applied to the coils. The discrepancy above −0.2 m is due to the residual magnetization of the magnet.

adiabatic spin rotation have been performed. The magnetic field profile in the three directions has been measured and used in these simulations, for which the total field strength along the beamline was shown in Fig. 10.

Quantum mechanical calculations, starting from the interaction Hamiltonian including the hyperfine interaction and the two Zeeman interactions with $\vec{I}$ and $\vec{J}$ are performed. The used Hamiltonian is of the

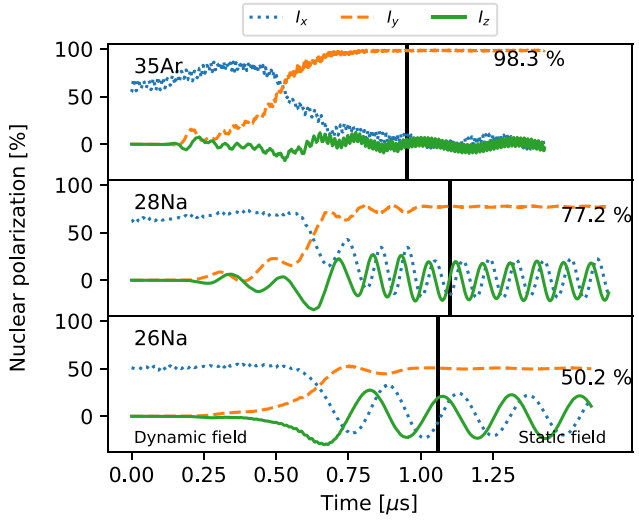

Fig. 11. Calculated change in the nuclear spin polarization along the x, y and z directions (dotted, dashed and full lines) due to the spin rotation from along the beam axis (x) to along the main field axis (y). The black full lines indicate the time at which the crystal site is reached by the beam: differences are due to mass and kinetic energy differences.

form

$$\mathcal{H}(t) = A\vec{I}\cdot\vec{J} + g_L\mu_b\vec{B}\cdot\vec{J} - g\mu_N\vec{B}\cdot\vec{I}, \tag{5}$$

where A is the magnetic dipole hyperfine parameter, $\vec{B}$ is the magnetic field vector, $\vec{I}$ and $\vec{J}$ are the nuclear and electron angular momenta, g and g_L are the nuclear and Landé g-factor respectively and μ_B and μ_N are the Bohr and nuclear magnetons.

A similar Hamiltonian has been studied before in the context of particles moving through a magnetic field, resulting in a time-varying field in the reference frame of the particle [25]. The derived differential equations have been solved for the explicit case of a constant magnetic field precessing about the z-axis. Here, the magnetic interaction between the spins $A\vec{I}\cdot\vec{J}$ has been added. The simulation code was written for use with QuTiP [26] which generates and solves the Hamiltonian for arbitrary nuclear species, each having different g-factors, spins and hyperfine parameters. The measured magnetic field is included in this Hamiltonian.

The state vector is initialized in the atomic ground state with populations in the $\vec{F}$ and m_F states as given by the rate equations after the optical pumping process. The interaction strength of the magnetic field represents the changing magnetic field as the particle beam travels through the setup at a certain speed. The measured magnetic field as plotted in Fig. 10 is used as input for $\vec{B}$, aside from the first few cm of flight path. Here, the magnetic field components perpendicular to the beamline have been suppressed. Around 0.1 μs, the perpendicular components are no longer suppressed and the spin vectors start precessing around the magnetic field. The varying oscillation periods for the simulated isotopes are mainly due to the different hyperfine interaction strengths. The spin dynamics are then calculated by solving the Schrödinger equation with the previous Hamiltonian. Experimental values for nuclear parameters in these equations were taken from Refs. [27,28]. The calculated flight time for the beam from the start of the transitional magnetic field to the implantation host is extended to also include a period where the beam is stopped in the host. The first period (the *dynamic* field region) is 2/3 of the total time solved for, while the implanted period (the *static* field region) accounts for 1/3 of the time. More details of the calculation can be found in Ref. [12].

The validity of the simulations has been verified by comparing the observed asymmetries for ^{26,28}Na to the asymmetry calculated on the one hand by the rate equations (neglecting spin rotation) and on the other hand from the quantum mechanical simulations that include the spin rotation process. Fig. 11 shows the calculated projection of the nuclear spin as a function of time along the three axes. Averaged over the implanted period, the nuclear spin projection along the main field axis (dashed line) is calculated to be 77% for ^{28}Na and 50% for ^{26}Na.

Table 2
Calculated and observed nuclear spin polarization of ^{26,28}Na. Experimental data taken from Ref. [6]. The quantum mechanical calculation is the average y polarization in Fig. 11 after implantation, the rate equation results are from a direct application of the adiabatic approximation to the rate equation populations.

	QM calc.	Rate equation	Experiment
^{28}Na	77%	83%	59%
^{26}Na	50%	58%	39%
Ratio	1.54	1.43	1.51

Table 3
The hyperfine parameters of ^{35}Ar, deduced from the measured hyperfine parameters of ^{39}Ar in the same laser transition [31] and the known ^{35}Ar nuclear moments [28].

	A [MHz] (calc.)	B [MHz] (calc.)
$1s_5$ $(J=2)$	265.8(28)	83(25)
$2p_9$ $(J=3)$	125.6(12)	80(19)

Table 2 presents the calculated nuclear spin polarization from both the rate equations assuming perfect adiabatic rotation and the quantum mechanical calculations. The observed asymmetry ratio between ^{26}Na and ^{28}Na matches the quantum mechanical calculation, although the absolute number is too high.

Simulations have also been made for the adiabatic rotation of maximally polarized ^{35}Ar (top panel of Fig. 11, see next section for details), indicating no loss in nuclear spin polarization from the rotation process.

7. Multiple-frequency pumping

For most elements, it is not possible to achieve 100% nuclear spin polarization using only one laser frequency in the pumping process. E.g. in the case of ^{35}Ar, one of the isotopes envisaged for fundamental interaction studies [4], simulations show that the maximum achievable nuclear spin polarization using a single laser transition is 67% for a laser power density of 80 mW/cm^2. This pumping scheme uses the 811 nm atomic transition ($1s_5 \rightarrow 2p_9$) that starts from the metastable $(1s_5)J=2$ state which is populated in the charge exchange process [29]. The hyperfine interaction with the nuclear spin of 3/2 leads to the metastable population being distributed among four hyperfine levels (see Fig. 12). Thus, when using only one laser transition in the optical pumping process, the maximum achievable atomic (and nuclear) spin-polarization will be limited. This can be overcome by using multi-frequency optical pumping to simultaneously excite more than one hyperfine transition. The same concept has already been applied at the TRIUMF facility for the polarization of Li, where EOM's were used to induce side-frequencies in the range of ±400 MHz to the main laser beam frequency [30].

In order to estimate the possible gain in nuclear polarization using multiple-frequency pumping, we performed simulations using the rate equations (details to be found in Ref. [12]). In these simulations, the nuclear spin polarization is calculated as a function of laser frequency, assuming optical pumping with two additional laser frequencies. The simulations have been performed for ^{35}Ar, the hyperfine parameters of which have been estimated (Table 3) based on its known nuclear moments [28] and the known hyperfine parameters of ^{39}Ar [31]. Adding two laser frequencies, at +325 MHz and +378 MHz from the main frequency (indicated in red in Fig. 12), it was found that by tuning the fundamental beam frequency to the $7/2 \rightarrow 9/2$ transition, nearly 100% nuclear polarization can be achieved, much higher than the 67% estimated for excitation with a single laser frequency.

This was verified experimentally, using a ^{35}Ar beam produced by a 1.4 GeV beam onto a CaO target at ISOLDE. The multi-frequency

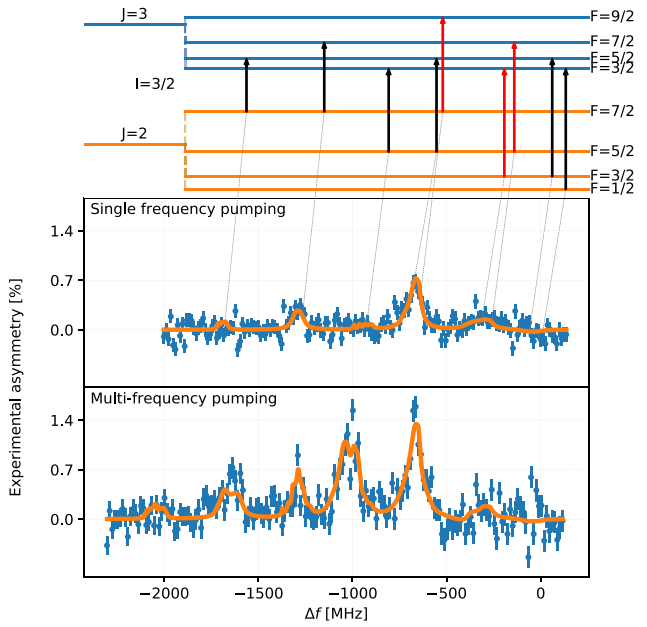

Fig. 12. Top: Hyperfine structure of the 811 nm transition with indicated allowed transitions. Using the hyperfine transitions $7/2 \rightarrow 9/2$, $5/2 \rightarrow 7/2$ and $3/2 \rightarrow 3/2$ (marked in red) saturates the polarization of the ensemble. Bottom plots: experimental spectra for both single- and multi-frequency pumping. Both spectra were fitted simultaneously to the rate equations. The laser power in the main beam was set to be a shared fit parameter, while the hyperfine parameters were fixed to the derived value (see Table 3). The transitions in the top are connected with their location in the single-frequency pumping spectrum. The x-axis gives the change in frequency of the fundamental laser beam, resulting in additional peaks in the multi-frequency spectrum at ~ 400 MHz to the left of each peak . (For interpretation of the references to color in this figure legend, the reader is referred to the web version of this article.)

pumping was realized by using two acousto-optic modulators (AOMs), which can each produce a side band frequency in the required ranges of 300–400 MHz by applying a fixed RF-frequency to the crystal inside the AOM. This shifts the frequency of the incoming laser light by the same value. For details on the setup of the AOMs, see Ref. [12].

The observed hyperfine spectra, using either one laser frequency or all three laser frequencies simultaneously, are shown in Fig. 12. The frequencies were varied by scanning the voltage applied to the voltage scanner, thus scanning all incident laser frequencies simultaneously. The induced nuclear spin-polarization is observed by measuring the asymmetry in the radioactive β-decay after implantation in a suitable crystal, as outlined before. The spectra shown in Fig. 12 have been recorded by implanting the polarized ^{35}Ar beam into a NaCl crystal kept at a temperature of 15(5) K, where the relaxation time was observed to be longer than the halflife of ^{35}Ar (1.78 s). The signal height in both spectra is significantly different, as can be seen clearly in e.g. the $7/2 \rightarrow 9/2$ transition, for which the observed asymmetry increases by almost a factor of 2.

In order to quantify the observed gain in signal strength (and thus spin-polarization), the data have been fitted using the rate equations that were implemented using the SATLAS Python package [32]. In the fitting procedure, the laser power (determining the linewidths), the centroid of the spectrum and the scaling (which the entire spectrum is multiplied with) were left as free parameters, while the A and B factors as given in Table 3 were kept as fixed values. Both spectra were fit simultaneously with the same value for the laser power, thus ensuring the correlations due to shared parameters were propagated correctly when determining the ratio of the signal strengths.

Excellent agreement is found between the observed spectra and the calculated β-asymmetry spectra as a function of the laser frequency, both for the single and triple laser–atom interaction systems. This gives confidence in the predictive power of this simulation package, such that it can be used in the future to optimize the laser polarization experiments. From the fitted signal strengths in both spectra, we find an increase in polarization of a factor 1.85(3).

The maximal asymmetry signal that can be observed requires careful evaluation of the ϵA term in the angular distribution. The asymmetry parameter A is known to be 0.43 [33]. The observed asymmetry is further reduced by several factors, all included in the ϵ. That includes the distribution of the ensemble among the different fine structure levels after charge exchange [34] and the solid angle coverage of the β-detectors. The evaluation of these factors is still ongoing. Note that the observed β-asymmetry in the largest peak amounts to nearly 1.5% using all three laser beams for pumping. The asymmetry observed here is comparable to the asymmetry observed in a previous study [35]. There, using momentum selection in fragmentation reactions to select a polarized beam, an asymmetry on the order of 0.5%–1% was observed in KBr at 20 K.

8. Conclusion

To answer the demand for accessible spin-polarized radioactive nuclei, the VITO beamline at ISOLDE was built as a dedicated setup. It is an adaptable beamline delivering highly polarized nuclei to a central detection point.

Beamline simulations agree with the observed transmission efficiency of 60%. The experimentally observed beamsteering effect seen for both designs of the voltage scanner is explained by the simulations.

The series of magnetic fields provide an efficient adiabatic rotation and decoupling of the nuclear spin. Rotation calculations agree with the observed asymmetry ratios. The rotation calculations can be repeated for different species provided the necessary nuclear parameters are available.

Finally, multi-frequency pumping has been established as a viable technique to increase the asymmetry signal that can be expected from the radioactive species. Tests on ^{35}Ar show that the increase and spectrum can be reproduced by the rate equation model.

Acknowledgments

This work was supported by the ERC Starting Grant no. 640465, FWO-Vlaanderen (Belgium), GOA 15/010 from KU Leuven, the Science and Technology Facilities Council (UK), the European Union's Horizon 2020 research and innovation programme grant agreement No 654002, and the Ministry of Education of Czech Republic (grant LM2015058).

References

[1] C.S. Wu, E. Ambler, R.W. Hayward, D.D. Hoppes, R.P. Hudson, Phys. Rev. 105 (1957) 1413–1415, http://dx.doi.org/10.1103/PhysRev.105.1413.

[2] R.F. Garcia Ruiz, M.L. Bissell, A. Gottberg, M. Stachura, L. Hemmingsen, G. Neyens, N. Severijns, EPJ Web Conf. 93 (2015) 07004, http://dx.doi.org/10.1051/epjconf/20159307004.

[3] M. Kowalska, V. Araujo Escalona, M. Baranowski, J. Croese, L. Cerato, M. Bissell, W. Gins, F. Gustafsson, R. Harding, L. Hemmingsen, H. Heylen, F. Hofmann, A. Kanellakopoulos, V. Kocman, M. Kozak, M. Madurga Flores, G. Neyens, S. Pallada, J. Plavec, K. Szutkowski, M. Walczak, F. Wienholtz, J. Wolak, X. Yang, D. Zakoucky, Interaction of Na+ ions with DNA G-quadruplex structures studied directly with Na beta-NMR spectroscopy, Technical Report CERN-INTC-2018-019, INTC-P-521-ADD-1, CERN, Geneva, 2018.

[4] P. Velten, M.L. Bissell, G. Neyens, N. Severijns, Measurement of the β-asymmetry parameter in^{35}Ar decay with a laser polarized beam, Technical Report CERN-INTC-2014-062, INTC-P-426, CERN, Geneva, 2014.

[5] C. Levy, A. Hatakeyama, Y. Hirayama, R. Kiefl, R. Baartman, J. Behr, H. Izumi, D. Melconian, G. Morris, R. Nussbaumer, M. Olivo, M. Pearson, R. Poutissou, G. Wight, Nucl. Instrum. Methods Phys. Res. B (2003) 689–693, http://dx.doi.org/10.1016/S0168-583X(03)00485-3.

[6] M. Kowalska, P. Aschenbrenner, M. Baranowski, M.L. Bissell, W. Gins, R.D. Harding, H. Heylen, G. Neyens, S. Pallada, N. Severijns, P. Velten, M. Walczak, F. Wienholtz, Z.Y. Xu, X.F. Yang, D. Zakoucky, J. Phys. G: Nucl. Part. Phys. 44 (2017) 084005.

[7] A. Kastler, J. Opt. Soc. Amer. 47 (1957) 460–465, http://dx.doi.org/10.1364/JOSA.47.000460.

[8] W. Demtröder, Laser Spectroscopy - Basic Concepts and Instrumentation, Springer-Verlag, 1981.
[9] R. Neugart, J. Billowes, M.L. Bissell, K. Blaum, B. Cheal, K.T. Flanagan, G. Neyens, W. Nörtershäuser, D.T. Yordanov, J. Phys. G: Nucl. Part. Phys. 44 (2017) 064002, http://dx.doi.org/10.1088/1361-6471/aa6642.
[10] J.D. Jackson, S.B. Treiman, H.W. Wyld, Phys. Rev. 106 (1957) 517–521, http://dx.doi.org/10.1103/PhysRev.106.517.
[11] D.T. Yordanov, From^{27}Mg to^{33}Mg: transition to the Island of inversion (Ph.D thesis), Katholieke Universiteit Leuven, 2007, URL https://fys.kuleuven.be/iks/nm/files/thesis/phd-thesis-dtyordanovphd.pdf.
[12] W. Gins, Development of a dedicated laser-polarization beamline for ISOLDE-CERN (Ph.D. thesis), KULeuven, 2019, URL https://fys.kuleuven.be/iks/nm/files/thesis/thesis-wgins.pdf.
[13] E. Kugler, Hyperfine Interact. 129 (2000) 23–42, http://dx.doi.org/10.1023/A:1012603025802.
[14] E. Mané, J. Billowes, K. Blaum, P. Campbell, B. Cheal, P. Delahaye, K.T. Flanagan, D.H. Forest, H. Franberg, C. Geppert, T. Giles, A. Jokinen, M. Kowalska, R. Neugart, G. Neyens, W. Nörtershäuser, I. Podadera, G. Tungate, P. Vingerhoets, D.T. Yordanov, Eur. Phys. J. A 42 (2009) 503–507, http://dx.doi.org/10.1140/epja/i2009-10828-0.
[15] M. Stachura, A. Gottberg, K. Johnston, M.L. Bissell, R.F. Garcia Ruiz, J. Martins Correia, A.R. Granadeiro Costa, M. Dehn, M. Deicher, A. Fenta, L. Hemmingsen, T.E. Mølholt, M. Munch, G. Neyens, S. Pallada, M.R. Silva, D. Zakoucky, Nucl. Instrum. Methods Phys. Res. B 376 (2016) 369–373, http://dx.doi.org/10.1016/j.nimb.2016.02.030.
[16] M. Kowalska, D.T. Yordanov, K. Blaum, P. Himpe, P. Lievens, S. Mallion, R. Neugart, G. Neyens, N. Vermeulen, Phys. Rev. C 77 (2008) 1–11, http://dx.doi.org/10.1103/PhysRevC.77.034307.
[17] N. Bendali, H.T. Duong, P. Juncar, J.M. Saint Jalm, J.L. Vialle, J. Phys. B 19 (1986) 233–238.
[18] A.C.C. Villari, W. Mittig, Nucl. Instrum. Methods 179 (1981) 195–198.
[19] K. Kreim, M. Bissell, J. Papuga, K. Blaum, M.D. Rydt, R.G. Ruiz, S. Goriely, H. Heylen, M. Kowalska, R. Neugart, G. Neyens, W. Nö, M. Rajabali, R.S. Alarcón, H. Stroke, D. Yordanov, Phys. Lett. B 731 (2014) 97–102, http://dx.doi.org/10.1016/j.physletb.2014.02.012.
[20] C.J. Foot, Atomic Physics, in: Oxford Master Series in Physics, Oxford University Press, 2005.
[21] R.F. Garcia Ruiz, C. Gorges, M. Bissell, K. Blaum, W. Gins, H. Heylen, K. Koenig, S. Kaufmann, M. Kowalska, J. Kramer, P. Lievens, S. Malbrunot-Ettenauer, R. Neugart, G. Neyens, W. Nörtershauser, D.T. Yordanov, X.F. Yang, J. Phys. G: Nucl. Part. Phys. 44 (2017) 044003, http://dx.doi.org/10.1088/1361-6471/aa5a24.
[22] K. Floettmann, Phys. Rev. ST Accel. Beams 6 (2003) 034202, http://dx.doi.org/10.1103/PhysRevSTAB.6.034202.
[23] C.O.M.S.O.L., Multiphysics Reference Guide for COMSOL 5.2a, 2017.
[24] M. Keim, Messung der kernquadrupolmomente neutronenreicher natriumisotope (Ph.D. thesis), Uni Mainz, 1996.
[25] J. Schwinger, Phys. Rev. 51 (1937) 648–651, http://dx.doi.org/10.1103/PhysRev.51.648.
[26] J. Johansson, P. Nation, F. Nori, Comput. Phys. Comm. 184 (2013) 1234–1240, http://dx.doi.org/10.1016/j.cpc.2012.11.019.
[27] F. Touchard, J.M. Serre, S. Büttgenbach, P. Guimbal, R. Klapisch, M. de Saint Simon, C. Thibault, H.T. Duong, P. Juncar, S. Liberman, J. Pinard, J.L. Vialle, Phys. Rev. C 25 (1982) 2756–2770, http://dx.doi.org/10.1103/PhysRevC.25.2756.
[28] T. Mertzimekis, K. Stamou, A. Psaltis, Nucl. Instrum. Methods Phys. Res. A 807 (2016) 56–60, http://dx.doi.org/10.1016/j.nima.2015.10.096.
[29] A. Klein, B. Brown, U. Georg, M. Keim, Nuclear Phys. A 607 (1996) 1–22.
[30] C.D.P. Levy, M.R. Pearson, G.D. Morris, K.H. Chow, M.D. Hossain, R.F. Kiefl, R. Labbé, J. Lassen, W.A. MacFarlane, T.J. Parolin, H. Saadaoui, M. Smadella, Q. Song, D. Wang, Hyperfine Interact. 196 (2010) 287–294, http://dx.doi.org/10.1007/s10751-009-0148-9.
[31] J. Welte, F. Ritterbusch, I. Steinke, M. Henrich, W. Aeschbach-Hertig, M.K. Oberthaler, New J. Phys. 12 (2010) http://dx.doi.org/10.1088/1367-2630/12/6/065031.
[32] W. Gins, R.P. de Groote, M.L. Bissell, C. Granados Buitrago, R. Ferrer, K.M. Lynch, G. Neyens, S. Sels, Comput. Phys. Comm. 222 (2018) 286–294, http://dx.doi.org/10.1016/j.cpc.2017.09.012.
[33] N. Severijns, O. Naviliat-Cuncic, Phys. Scr. (2013) http://dx.doi.org/10.1088/0031-8949/2013/T152/014018.
[34] C. Ryder, K. Minamisono, H. Asberry, B. Isherwood, P. Mantica, A. Miller, D. Rossi, R. Strum, Spectrochim. Acta B 12 (2015) 16–21, http://dx.doi.org/10.1016/j.sab.2015.08.004.
[35] K. Matsuta, T. Tsubota, C. Ha, T. Miyake, Nuclear Phys. A 701 (2002) 383–386.